Journal of Alloys and Compounds 611 (2014) 179–190

Contents lists available at ScienceDirect

Journal of Alloys and Compounds

journal homepage: www.elsevier.com/locate/jalcom

Mechanical and electrochemical properties of nanocrystalline $(Mo_{1-x}Cr_x)_3Si$ coatings: Experimental and modeling studies

Jiang Xu [a,b,*], ZhengYang Li [c], Xiaolin Lu [a], Yong Yan [d], Paul Munroe [e], Zong-Han Xie [b,f]

[a] Department of Material Science and Engineering, Nanjing University of Aeronautics and Astronautics, 29 Yudao Street, Nanjing 210016, PR China
[b] School of Mechanical & Electrical Engineering, Wuhan Institute of Technology, 693 Xiongchu Avenue, Wuhan 430073, PR China
[c] Institute of Mechanics, Chinese Academy of Sciences, Beijing 100190, PR China
[d] Huangshi Coal Mining Bureau Hospital, 501 Lakeside Road, Huangshi 435001, PR China
[e] School of Materials Science and Engineering, University of New South Wales, NSW 2052, Australia
[f] School of Mechanical Engineering, University of Adelaide, SA 5005, Australia

ARTICLE INFO

Article history:
Received 24 February 2014
Received in revised form 13 May 2014
Accepted 14 May 2014
Available online 22 May 2014

Keywords:
Intermetallic
EIS
Polarization
First-principle calculation

ABSTRACT

Four $(Mo_{1-x}Cr_x)_3Si$ nanocrystalline coatings with a cubic A15 structure were fabricated onto Ti–6Al–4V substrates using a double-cathode glow discharge technique. The elastic modulus and hardness of the nanocrystalline $(Mo_{1-x}Cr_x)_3Si$ coatings were measured by nanoindentation and their electrochemical behavior was investigated by potentiodynamic polarization and electrochemical impedance spectroscopy (EIS) in a 3.5 wt% NaCl solution. The results showed that the corrosion and abrasion damage resistance of the nanocrystalline $(Mo_{1-x}Cr_x)_3Si$ coatings increased with increasing Cr addition. To gain a deeper understanding of the effect of Cr alloying on the electrochemical behavior of these $(Mo_{1-x}Cr_x)_3Si$ coatings, the electronic structure and Mulliken populations were modeled by first-principles calculations. It revealed that the Cr alloying can enhance the protective nature of passive layers developed on the Mo_3Si coatings. The findings provide a promising foundation for the development of mechanically robust, corrosion-resistant Mo_3Si-based coatings for surface protection.

1. Introduction

Corrosion of materials is pervasive and responsible in part for degradation of components during long-term service. Corrosion damage can lead to huge economic losses and inflict harmful effects on safety and livelihood. Preparing a protective coating using various surface modification methods is regarded as one of the most economical and effective ways to improve the long-term corrosion resistance of materials in service environments [1,2]. Molybdenum silicides offer some advantageous mechanical and physical properties, such as high melting point, good hardness, excellent high oxidation resistance and thermal conductivity [3–6], which are essential to make them attractive as wear and corrosion resistant coating materials suitable for extremely harsh working conditions. Unfortunately, similar to other intermetallic compounds, these silicides have a number of undesirable properties including poor low temperature oxidation resistance and room-temperature brittleness, which are currently two major obstacles that inhibit their practical application [7]. To overcome these problems, several strategies based on either forming multiphase composites or substitutional alloying have been explored and some results have been hitherto relatively satisfactory [8,9]. Nevertheless, one aspect of molybdenum silicides that is equally important for structural application is their electrochemical behavior in corrosive electrolytic media and this remains poorly understood.

In the Mo–Si binary phase diagram, there are three compounds, i.e., $C11_b$ structured $MoSi_2$, D8m-structured Mo_5Si_3, and A15-structured Mo_3Si. There has been significant study devoted to monolithic $MoSi_2$ and Mo_5Si_3, as well as their composites, in the past decades, specifically $MoSi_2$, but Mo_3Si has received limited attention, with the exception of a small number of studies regarding its wear performance and mechanical properties [10–12]. To the best of our knowledge, there are no reports available in the literature with regard to the performance of Mo_3Si in corrosive media at ambient temperature, which is important for its structural application. In our previous work [13,14], $MoSi_2$ and Mo_5Si_3 nanocrystalline coatings have been successfully prepared onto Ti–6Al–4V substrates using a double-cathode glow discharge technique.

* Corresponding author at: Department of Material Science and Engineering, Nanjing University of Aeronautics and Astronautics, 29 Yudao Street, Nanjing 210016, PR China. Tel.: +86 2552112626.
E-mail address: xujiang73@nuaa.edu.cn (J. Xu).

http://dx.doi.org/10.1016/j.jallcom.2014.05.099
0925-8388/

Building on prior knowledge, in this work, $(Mo_{1-x}Cr_x)_3Si$ (x = 0, 0.09, 0.20 and 0.29) nanocrystalline coatings with a cubic A15 structure were fabricated onto Ti–6Al–4V substrates using the same technique. The influence of Cr additions on the elastic modulus and hardness of the $(Mo_{1-x}Cr_x)_3Si$ nanocrystalline coatings were measured by nanoindentation. The electrochemical behavior of the nanocrystalline $(Mo_{1-x}Cr_x)_3Si$ coatings were evaluated by potentiodynamic polarization and electrochemical impedance spectroscopy (EIS), to uncover the effects of Cr alloying on the corrosion behavior of Mo_3Si. Moreover, electronic structure and Mulliken populations were calculated based on the first principles density-functional theory, providing guidance to elucidate the roles of Cr on the chemical bonding of Mo_3Si that control the surface composition and corrosion resistance of the passive films on $(Mo_{1-x}Cr_x)_3Si$ nanocrystalline coatings.

2. Experimental methods and computational details

2.1. Specimen preparation

Disk-shaped substrates, 40 mm in diameter and 3 mm thick, were cut from Ti–6A1–4V rods. The chemical composition of this alloy in wt% is: Al, 6.04; V, 4.03; Fe, 0.3; O, 0.1; C, 0.1; N, 0.05; H, 0.015 and the balance, Ti. Prior to deposition, the substrates were successively ground with a series of silicon carbide papers and finally polished with 1.5 μm diamond paste to obtain a mirror-like surface finish. The polished substrates were then ultrasonically cleaned in ethyl alcohol and dried in cold air. Four $(Mo_xCr_{1-x})_3Si$ (x = 0, 0.09, 0.20, 0.29) nanocrystalline coatings were deposited onto the polished substrates using a double cathode glow discharge using four targets with different stoichiometric ratios ($Mo_{75}Si_{25}$, $Mo_{65}Cr_{10}Si_{25}$, $Mo_{55}Cr_{20}Si_{25}$ and $Mo_{45}Cr_{30}Si_{25}$), respectively. The reason for such a difference in the composition of the targets and the deposited coatings is that the composition of the coatings is related to not only the composition of target materials, but also the relative sputtering yields of the alloying elements in the targets. Furthermore, diffusion of alloying elements at the interface between the coatings and substrates also affects the composition of the films. Inside the chamber, one cathode is used as the target, and the other as the substrate, as described elsewhere [15,16]. The sputtering targets were fabricated from ball-milled Mo (99.99% purity), Cr (99.99% purity) and Si powders (99.99% purity) by employing cold compaction under a pressure of 600 MPa. The glow discharge sputtering conditions are given as follows: base pressure, 4×10^{-4} Pa; target electrode bias voltage, −900 V; substrate bias voltage, −350 V; substrate temperature, 900 °C; working pressure(Ar gas), 35 Pa; parallel distance between the source electrode and the substrate, 15 mm and treatment time of 5 h.

2.2. Phase identification and microstructure characterization

The phase compositions of the as-deposited coatings were analyzed by an X-ray diffractometer (XRD, D8 ADVANCE with Cu Kα radiation) operating at 35 kV and 40 mA. X-ray spectra were collected in the 2θ range from 20° to 90° at a scan rate of 0.5°/min. The cross-sectional morphologies and chemical composition of the as-prepared coatings were examined by a field emission scanning electron microscope (FESEM, Hitachi, S-4800, Japan) equipped with an energy-dispersive X-ray spectrometer (EDS). The sectioned coatings were etched using Kroll's reagent (1% HF, 2% HNO_3 and 97% H_2O) for 30 s to obtain good contrast of the coating/substrate interface. The microstructural features of the as-deposited coatings were observed using transmission electron microscopy (TEM, Tecnai G220, FEI Company) at an accelerating voltage of 200 kV. The plan-view samples for TEM observation were also prepared using a single-jet electro-chemical polishing technique from the untreated side of the substrate.

2.3. Nanoindentation tests

The indentation hardness and elastic modulus of the as-deposited coatings were obtained using a nanoindentation tester (NHT) with a Berkovich diamond indenter. This system, developed by CSEM Instruments, comprises two major components: a measuring head for performing nanoindentation and an optical microscope for selecting a specific location prior to indentation, and for checking the location of the imprint after indentation. The system has load and displacement resolutions of 10 μN and 1 nm, respectively. Fused silica was used as a standard sample for the tip calibration. The indentation was performed by driving the indenter at a constant loading rate of 40 mN min^{-1} into the material surface with the maximum applied load of 20 mN. Hardness and the elastic modulus were evaluated using the Oliver–Pharr method [17] based on the load–displacement data obtained during the indentation tests. Ten indentations were made for each sample to ensure repeatability of the experimental data.

2.4. Electrochemical measurements and XPS analysis

Electrochemical measurements (CHI 660C, Shanghai, China) were conducted in a standard three-electrode cell, consisting of a working electrode (WE) made from a coating specimen with a 1.0 cm^2 exposed area, a platinum counter electrode (CE), and a saturated calomel reference electrode (SCE). The electrolyte used was 3.5 wt% NaCl solution open to air, which was prepared from reagent grade chemical and distilled water. The potentiodynamic polarization curves were recorded at a sweep rate of 20 mV min^{-1}, starting from the moment when the open circuit potential (OCP) reached its steady state after immersing the specimen in the electrolyte for about 30 min. Electrochemical impedance spectroscopy (EIS) measurements were carried out using an excitation signal of 10 mV peak-to-peak over a frequency range from 100 kHz extending up to 10 mHz at the respective OCPs. The EIS experimental data were analyzed and fitted to appropriate electrical equivalent circuit (EEC) using the ZSimpWin software.

X-ray photoelectron spectroscopy (XPS) analysis was carried out on the four coatings after potentiostatic polarization at a potential of 0.1 V_{SCE} for 60 min in 3.5 wt% NaCl solution open to air at 25 °C. XPS measurements were carried out using a Kratos AXIS Ultra ESCA system with an Al Kα (1486.71 eV) X-ray source. The accelerating voltage and emission current of the X-ray source were kept at 12 kV and 12 mA, respectively. The base pressure of the sample chamber was maintained at $\sim 10^{-10}$ Torr. The pass energy was selected at 80 eV for survey scan and 10 eV for the features of interest (i.e., O 1s, Mo 3d and Si 2p) to ensure high resolution and good sensitivity. All the binding energy values were calibrated against the C 1s peak of hydrocarbon contamination fixed at 284.6 eV. Quantitative analysis of the XPS experimental data was carried out using Casa XPS-Version 2.3.14. A Shirley background correction was employed for background subtraction for each high resolution spectrum. The decoupling of spectra was performed using Gaussian function with zero asymmetry indexes. The relative sensitivity factors for each element were obtained from standard database of the Casa XPS software.

2.5. Theoretical models and computational details

First-principles calculations were employed to analyze the influence of Cr alloying on the strength of the interatomic bonds in $(Mo_{1-x}Cr_x)_3Si$. The calculations were carried out using the first principles methods based on the density functional theory as implemented in the CASTEP code [18]. The interactions between the ionic cores and the electrons were described by ultrasoft pseudo-potentials [19], in which the orbital electrons of Mo-$4s^24p^64d^55s^1$, Cr-$4s^24p^63d^54s^1$ and Si-$3s^23p^2$ were treated as valence electrons. To confirm the convergence of the calculations for the Brillouin-zone sampling, the dependence of the total energy on the plane wave cut-off energy and the k-point mesh was examined according to the Monkhorst–Pack grid scheme [20]. To generate compositions close to experimental stoichiometries, a $2 \times 2 \times 2$ supercell consisting of 64 atoms was constructed for A15-structured $(Mo_{1-x}Cr_x)_3Si$, where Mo atoms were replaced by 4, 8 and 12Cr atoms and the corresponding Cr concentrations (i.e., 'x' value) were 0.083, 0.167 and 0.250 (see Fig. 1(a–d)), respectively. An energy cut-off of 450 eV and a $6 \times 6 \times 6$ k-point set were used for all the calculations [21]. The equilibrium lattice parameter was computed from a structural optimization, using the Broyden Fletcher Goldfarb Shanno (BFGS) minimization technique, which provides a rapid way to find the lowest energy structure [22]. In the structural optimization process, the energy change, maximum force, maximum stress, and maximum displacement tolerances were set as 5.0×10^{-6} eV/atom, 0.01 eV/Å, 0.02 GPa and 5.0×10^{-4} Å, respectively [23]. The Mulliken population is an objective and quantitative criterion to characterize the relative strength of chemical bonds, i.e. the higher the Mulliken bond population, the stronger the chemical bonds. Mulliken population defined by:

$$M_{ab} = 2\sum_{j}\sum_{j,k} C_{ja,i} C_{Kb,i} S_{ja,kb} \quad (1)$$

where $\sum_i$ and $\sum_{j,k}$ are summations over occupied states and over basis functions on atoms a and b, respectively. $C_{ja,i}$ is the coefficient of the jth atomic orbital of the atom a composing the ith molecular orbital. $C_{kb,i}$ is the coefficient of the kth atomic orbital of the atom b composing the ith molecular orbital. $S_{ja,kb}$ is the overlap matrix element between atomic orbitals of a and b, which is affected by their interatomic distance. The value of M_{ab} reflects the charge and interatomic distance between the two atoms.

3. Results

3.1. Microstructure and phase analysis

Fig. 2 presents typical X-ray diffraction patterns recorded from the four $(Mo_{1-x}Cr_x)_3Si$ (x = 0, 0.09, 0.20 and 0.29) coatings deposited on Ti–6Al–4V substrates. It is evident from Fig. 2 that three broad diffraction peaks of the as-prepared coatings respectively can be indexed to the (200), (210) and (321) planes of the cubic A15-structured Mo_3Si (JCPDS Card No. 51-0764). Compared with

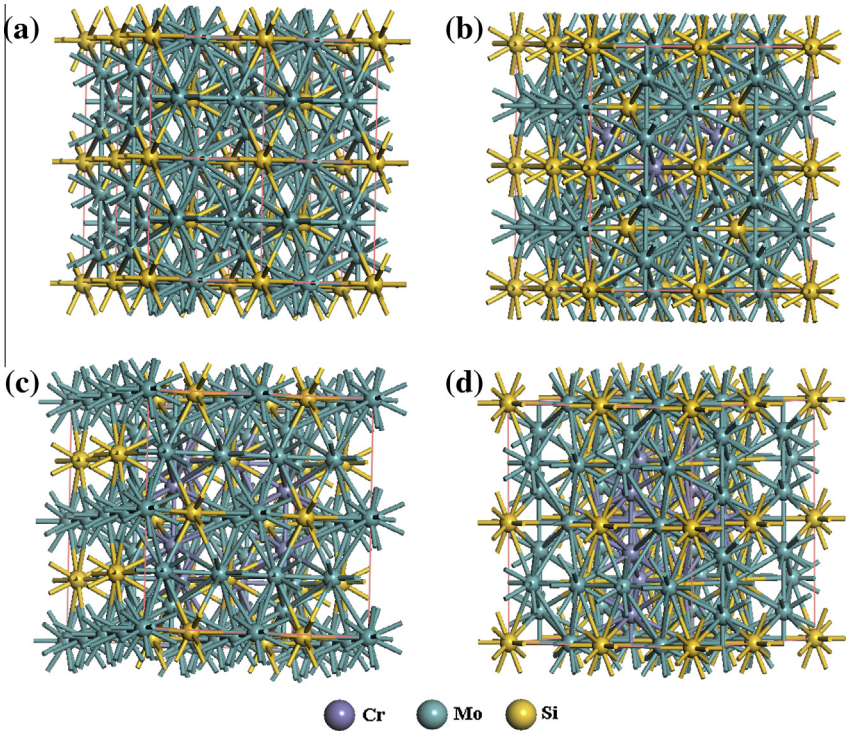

Fig. 1. The optimized structures of (a) Mo_3Si; (b) $(Mo_{0.917}Cr_{0.083})_3Si$; (c) $(Mo_{0.833}Cr_{0.167})_3Si$; (d) $(Mo_{0.750}Cr_{0.250})_3Si$.

those of the binary Mo_3Si coating, the diffraction peaks of the three Cr-containing Mo_3Si compounds gradually shift to higher diffraction angles with increasing Cr concentration. Moreover, with increasing Cr content, the intensity of the (200) peak increases, whereas the intensities of the (210) and (321) peaks decrease accordingly, indicative of a change in preferred orientation of the as-deposited coatings from (210) to (200) through Cr additions. From the intensity data, the preferred orientations of the $(Mo_{1-x}Cr_x)_3Si$ coatings were evaluated by the texture coefficient (TC_{hkl}) according to the following equation [24]:

$$TC_{hkl} = \frac{I_m(hkl)/I_0(hkl)}{\frac{1}{n}\sum_1^n I_m(hkl)/I_0(hkl)} \quad (2)$$

where $I_m(hkl)$ is the measured X-ray relative intensity of the (hkl) plane, $I_0(hkl)$ is the relative intensity in the powder pattern, (hkl) are the indices for the reflections and n is the number of reflection planes. For the TC_{hkl} value greater than 1, a preferred orientation is developed towards a crystalline plane; while the TC_{hkl} value is close to 1, signifying a random orientation and the TC_{hkl} value is in the range from 0 to 1, denoting a lack of grain orientation in the plane under consideration [25]. The variation of the texture coefficients with Cr content in the as-deposited coatings is shown in Fig. 3. Apparently, for the binary Mo_3Si coating, only the TC_{210} is larger than unity, whereas only the TC_{200} is larger than unity after the addition of Cr to Mo_3Si, suggesting that the preferred growth direction (i.e., parallel to the substrate normal) of the $(Mo_{1-x}Cr_x)_3Si$ coatings changes from (210) to (200) orientations through Cr addition. The evolution of preferred orientation for the films can be explained in terms of surface and strain energy contributions to total energy [26,27]. Because the four $(Mo_{1-x}Cr_x)_3Si$ coatings with similar thicknesses were fabricated under the identical experimental conditions, the discrepancy in strain energy, which is predominately

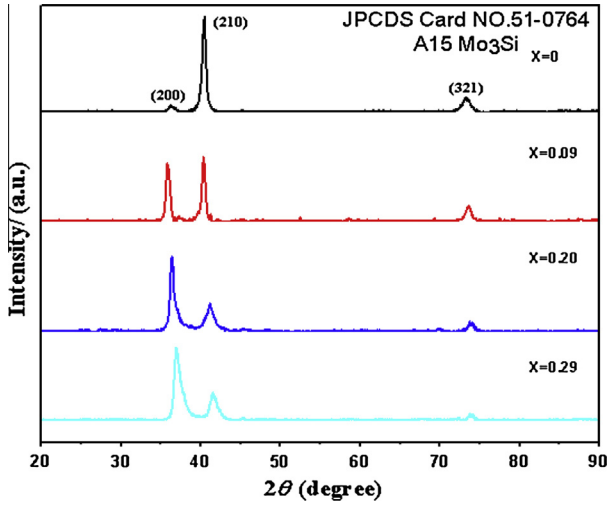

Fig. 2. XRD patterns of the $(Mo_{1-x}Cr_x)_3Si$(x = 0, 0.09, 0.20 and 0.29) nanocrystalline coatings.

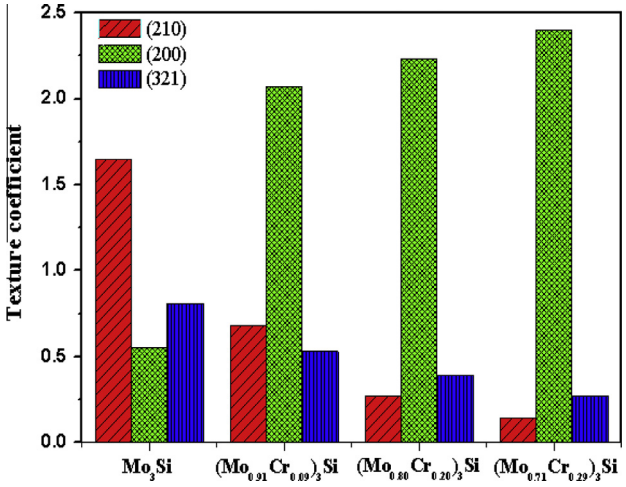

Fig. 3. The calculated texture coefficients for the $(Mo_{1-x}Cr_x)_3Si$ (x = 0, 0.09, 0.20 and 0.29) nanocrystalline coatings.

determined by coating thickness, is negligible among the resultant coatings. Thus, the surface energy becomes the dominant factor controlling the preferred orientation of the coatings arising from the incorporation of Cr to Mo_3Si. On the basis of the particular diffraction lines (200), (210) and (321), values of the lattice parameter were evaluated. Since the representation of particular crystallographic planes is proportional to the texture coefficient, the resulting lattice parameter was calculated as a weighted mean value from the formula:

$$a_{TC} = a_{200} \times TC_{200} + a_{210} \times TC_{210} + a_{321} \times TC_{321} \quad (3)$$

Fig. 4 shows values of the lattice parameter (lattice constants: $a = b = c$) obtained both through first principles calculations and XRD data, as a function of Cr content in the as-deposited coatings. Although there is a slight difference in the absolute values determined between calculation and experiment, the trends in change of the calculated lattice parameters are the same as that of the experimental data, i.e., the lattice constants of $(Mo_{1-x}Cr_x)_3Si$ decrease with increasing x values (i.e., Cr contents). Since the atomic size of Cr is smaller than that of Mo, the lattice parameters would decrease with the substitution of Cr for Mo sites in the crystalline structure of Mo_3Si.

Fig. 5 shows cross-sectional SEM images and elemental concentration profiles from EDS analyses of the $(Mo_{1-x}Cr_x)_3Si$ coatings deposited on Ti–6Al–4V substrates. Clearly, the four coatings exhibit a homogeneous and dense structure, without any defects visible across the entire coating thickness, and are securely anchored onto the Ti–6Al–4V substrates. The microstructure of these coatings is composed of a ~20 μm thick outer deposited layer and an inner diffusion layer with a thickness of ~15 μm. EDS analysis indicates that outer deposited layers have a Mo/Si or (Mo + Cr)/Si atomic ratio close to 3, consistent with being $(Mo_{1-x}Cr_x)_3Si$; the inner diffusion layers show a gradient distribution of the alloy elements across their depth and are highly enriched in Mo and Ti with minor amounts of Si, Cr, Al and V. Fig. 6(a and b) shows plan-view TEM bright-field/dark-field images of the deposited layer of the $(Mo_{0.91}Cr_{0.09})_3Si$ coating. It can be seen that the microstructure of the coating consists of slightly elongated grains with an average width of 10 nm. The associated selected area electron diffraction (SAED) (inset in Fig. 6(a)) can be identified as a cubic A15-structured Mo_3Si with the first three rings originating from the (200), (210) and (321) planes, respectively. The bright-field HRTEM lattice image shows that lattice fringes with a spacing of 2.17 Å (marked with circles) correspond to the d-spacing of the {210} planes for cubic A15-structured Mo_3Si.

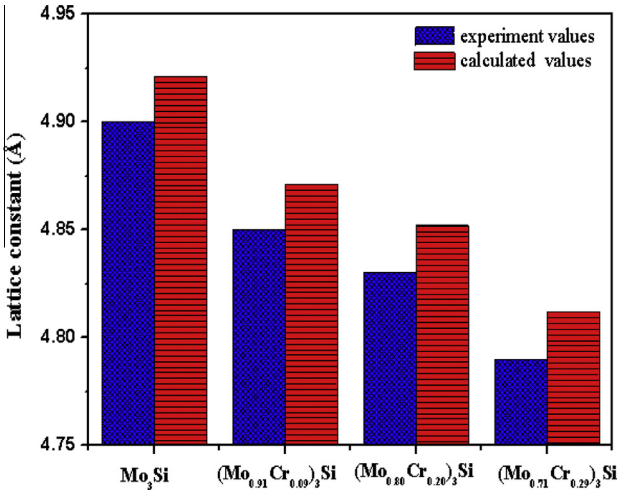

Fig. 4. The lattice constants of the $(Mo_{1-x}Cr_x)_3Si$ ($x = 0$, 0.09, 0.20 and 0.29) nanocrystalline coatings.

3.2. Nanoindentation tests

Typical load–displacement (p–h) curves obtained from instrumented nanoindentation for the four $(Mo_{1-x}Cr_x)_3Si$ coatings deposited on Ti–6Al–4V substrates indented with a maximum load of 20 mN are presented in Fig. 7(a). As can be seen from Fig. 7(a), the maximum indentation depths d_{max} increase with increasing Cr content, representing that resistance of the coatings to plastic deformation is reduced by Cr addition. Fig. 7(b) shows the variation of the hardness and elastic modulus with Cr content in the coatings. Owing to the d_{max} of the coatings being far less than 10% of the coatings thickness, the contribution to mechanical properties from the substrate is assumed to be negligible. As shown in Fig. 7(b), the hardness and elastic modulus of the four $(Mo_{1-x}Cr_x)_3Si$ ($x = 0$, 0.09, 0.20 and 0.29) coatings are inversely proportional to the Cr content in the coatings; in other words, lower hardness and elastic modulus values were found for higher Cr additions. It is worthwhile to note that the four $(Mo_{1-x}Cr_x)_3Si$ coatings show higher values of hardness than coarse-grained Mo_3Si ($H = 12.85$ GPa) reported by Misra et al. [6]. According to the hardness and modulus measurements, the threshold load for crack initiation of the coatings can be assessed, which varies directly with $1/E^2H$. This parameter has also used as an index to forecast tolerance to abrasion wear caused by micro-cracking [28]. As shown in Fig. 7(c), the $1/E^2H$ ratios of the four $(Mo_{1-x}Cr_x)_3Si$ coatings increase with increasing Cr concentration, indicating that the higher Cr content in the coatings, the greater the resistance of the coatings against abrasive wear. The mechanical properties for the cubic A15-structured Mo_3Si, including bulk modulus (B), shear modulus (G) and elastic modulus (E), were calculated based on the Voigt–Reuss–Hill approximation [29] and the calculated results are plotted in Fig. 8. As shown in Fig. 8, Cr alloying has no obvious impact on the values of shear modulus, but lowers the values of the bulk and elastic modulus. The values of the calculated elastic modulus closely approximate to the experimental values at a similar composition.

3.3. OCP and LF impedance vs time measurements

Fig. 9(a) shows the open-circuit potentials (E_{OCP}) of the four $(Mo_{1-x}Cr_x)_3Si$ coatings as a function of immersion time in 3.5 wt% NaCl solutions open to air at 25 °C. From the OCP–time curves, the E_{OCP} evolution of the coatings exhibits a similar feature: during the initial immersion stage, the E_{OCP} for the four as-deposited coatings shifts rapidly to a more noble direction with time, indicating that the formation and thickening of the naturally formed passive films on the four as-deposited coatings [30,31]; subsequently, the E_{OCP} becomes almost independent of immersion time, approaching a steady potential. With the increase in the Cr concentration, the time taken to attain a steady E_{OCP} is shorter and a more positive E_{OCP} can be achieved. Low-frequency (LF) impedance, as a key parameter describing the barrier properties of materials in a corrosive electrolyte, can assist in understanding the transport kinetics of aggressive species through materials [32]. It can be seen from the LF impedances ($|Z|_{f=1Hz}$)–time curves (Fig. 9(b)) that the modulus of the LF impedance of the four $(Mo_{1-x}Cr_x)_3Si$ coatings increase with Cr additions, suggesting that the incorporation of Cr into Mo_3Si enhances the corrosion protection ability of the coatings.

3.4. Potentiodynamic polarization measurements

Fig. 10 shows the representative potentiodynamic polarization curves of the four $(Mo_{1-x}Cr_x)_3Si$ coatings in 3.5 wt% NaCl solutions open to air at 25 °C. As the Cr content increases, the corrosion potentials (E_{corr} vs SCE) of the coatings move to more positive values, and the displacement of the anodic branches of the polarization curves is in the direction of the region of lower current

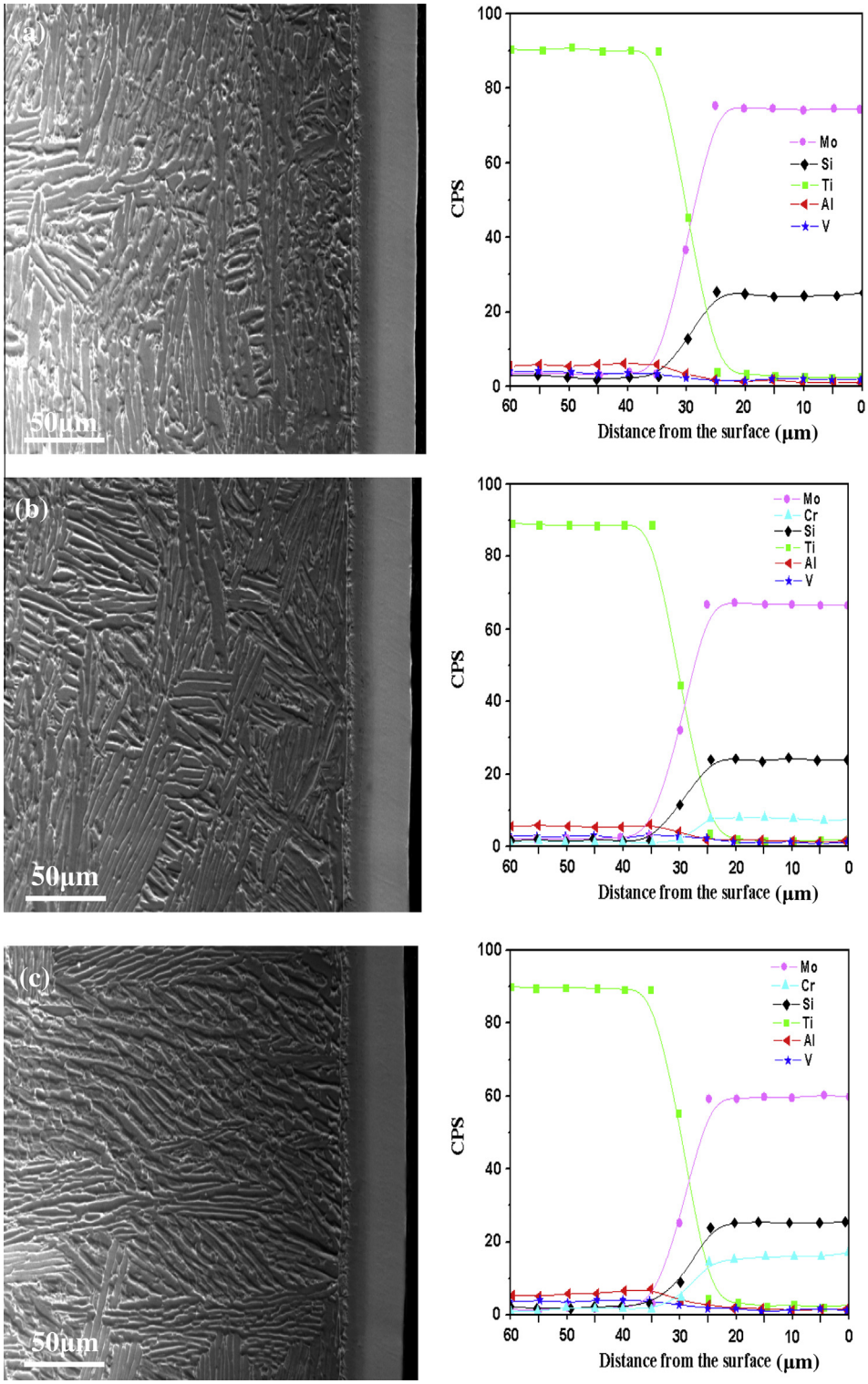

Fig. 5. SEM cross-sectional images and elemental concentration profiles from EDS analyses of the $(Mo_{1-x}Cr_x)_3Si$ nanocrystalline coatings: (a) $x = 0$; (b) $x = 0.09$; (c) $x = 0.20$; (d) $x = 0.29$.

density. Moreover, it is also found that the passive films grown on the four coatings are unstable, because the current density inside the anodic branches increases continuously with applied potential. For the binary Mo_3Si coating, the anodic current density increases abruptly after a short passivation range ($-300 \sim 150$ mV_{SCE}) on the anodic polarization curve, suggesting the occurrence of transpassive dissolution. This behavior may be due to the dissolution of the originally formed passive film on top of the Mo_3Si coating in the chloride-containing electrolyte. In the case of three Cr-containing Mo_3Si coatings, the slopes of the $\log i$–E plots in the anodic branches decrease with increasing Cr content, denoting a reduction of the dissolution rates of the passive layers.

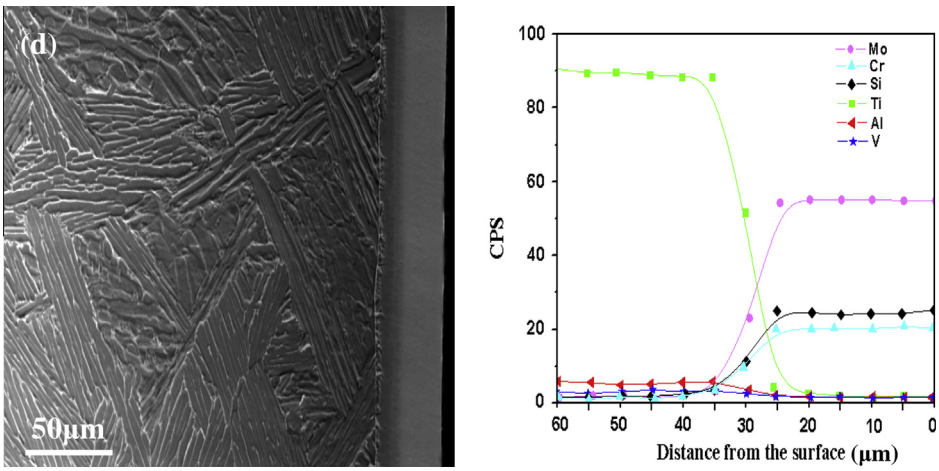

Fig. 5 (*continued*)

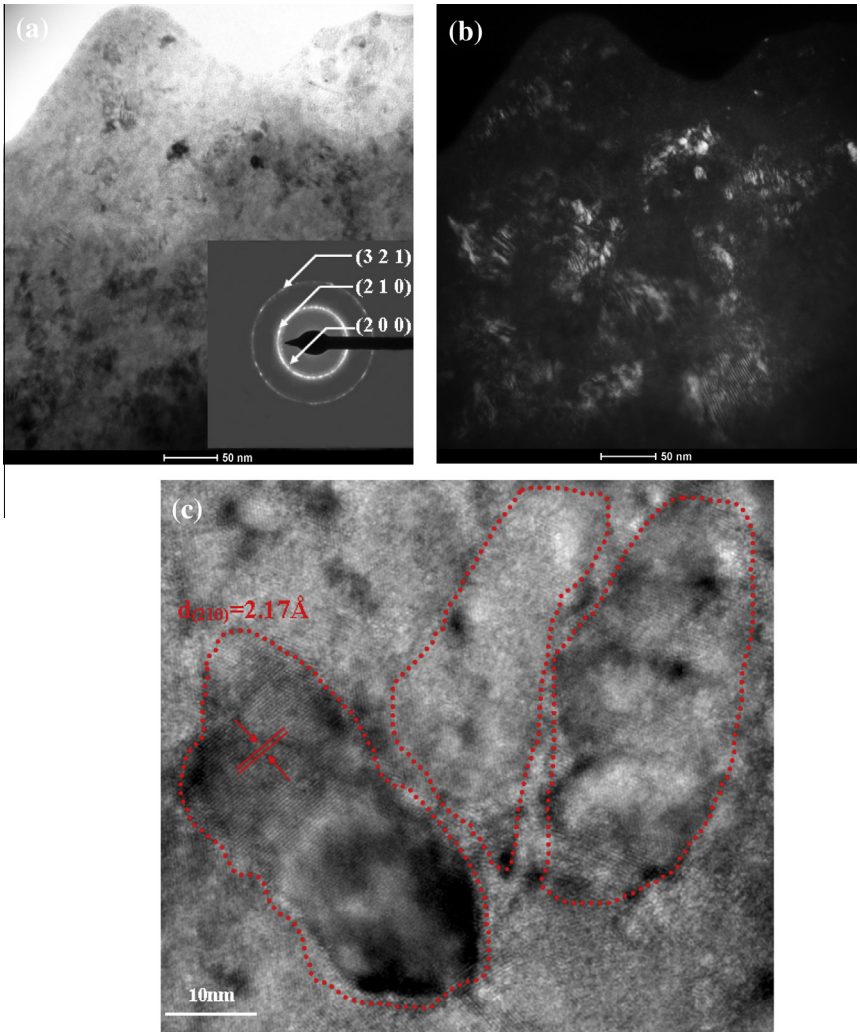

Fig. 6. Plan-view TEM bright-field (a) /dark-field (b) images of the $(Mo_{0.91}Cr_{0.09})_3Si$ nanocrystalline coating. (c) An HRTEM image of the $(Mo_{0.91}Cr_{0.09})_3Si$ nanocrystalline coating.

3.5. Electrochemical impedance spectroscopy (EIS)

Fig. 11(a and b) shows the Nyquist and Bode plots for the four $(Mo_{1-x}Cr_x)_3Si$ coatings in 3.5 wt% NaCl solution at their respective open circuit potentials, respectively. The Nyquist plots of the coatings display a single depressed capacitive semicircle in the entire frequency range and the diameter of the capacitive semicircles increases with Cr addition, indicating an increase in the corrosion

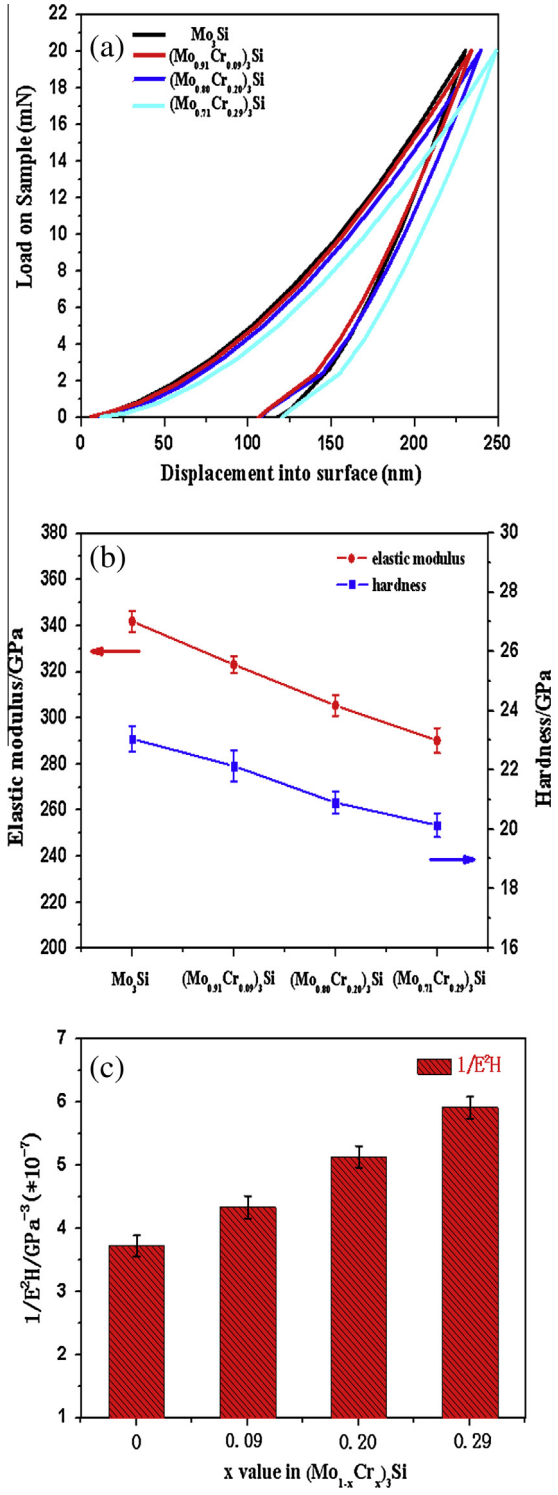

Fig. 7. (a) Load–displacement curves of the $(Mo_{1-x}Cr_x)_3Si$ nanocrystalline coatings; (b) elastic modulus and hardness of $(Mo_{1-x}Cr_x)_3Si$ nanocrystalline coatings as a function of Cr content; (c) the $1/E^2H$ ratios for the four nanocrystalline coatings.

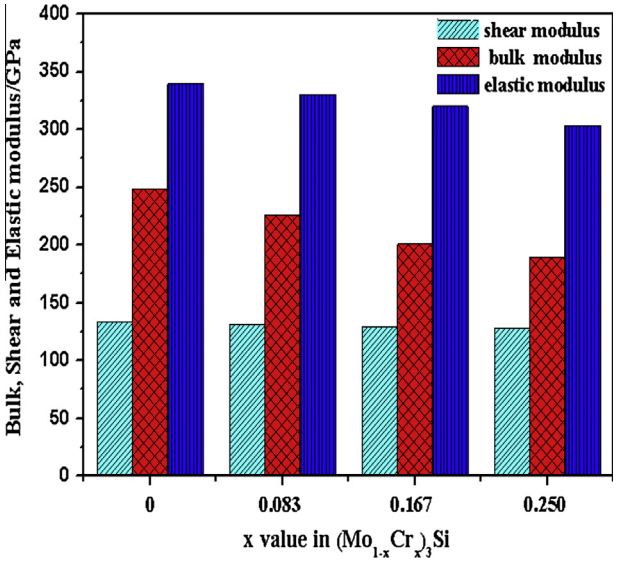

Fig. 8. The calculated bulk, elastic and shear modulus of the $(Mo_{1-x}Cr_x)_3Si$ nanocrystalline coatings.

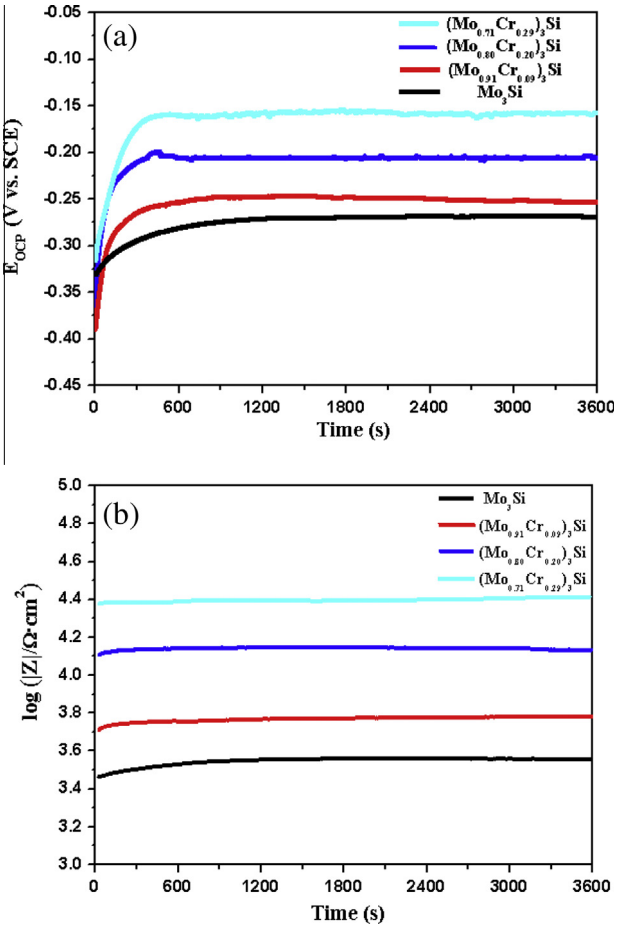

Fig. 9. (a) Open circuit potential (OCP) and (b) low-frequency (LF) impedance of the $(Mo_{1-x}Cr_x)_3Si$ nanocrystalline coatings in 3.5 wt% NaCl solution open to air at room temperature.

resistance of the $(Mo_{1-x}Cr_x)_3Si$ coatings by the incorporation of Cr. As shown in Fig. 11(b), the Bode plots of the four $(Mo_{1-x}Cr_x)_3Si$ coatings show an obvious capacitive behavior from medium to low frequencies [33–36], which is characterized by a maximum near −90° in the Bode-phase plots and a linear region with a slope close to −1 in the Bode-magnitude plots. It is evident that the magnitude of the impedance at very low frequencies ($|Z|_{f\to 0}$), the phase angle maximum, and the frequency range with the phase angle near −90° increase with Cr content, implying that the protection capacity of the passive films formed on the coatings is enhanced by Cr additions.

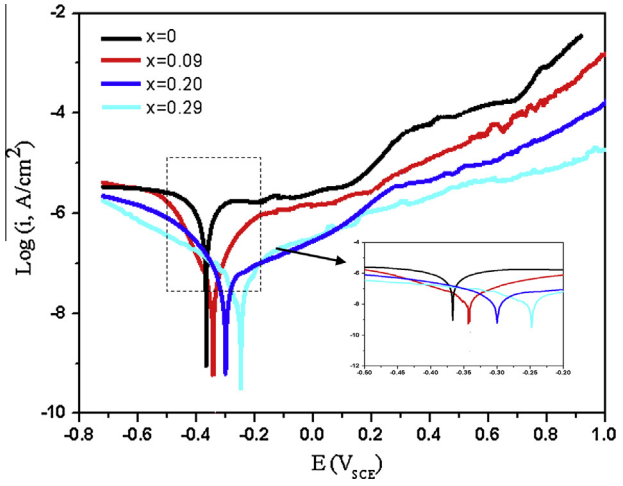

Fig. 10. Potentiodynamic polarization curves of the $(Mo_{1-x}Cr_x)_3Si$ nanocrystalline coatings in 3.5 wt% NaCl solution open to air at room temperature.

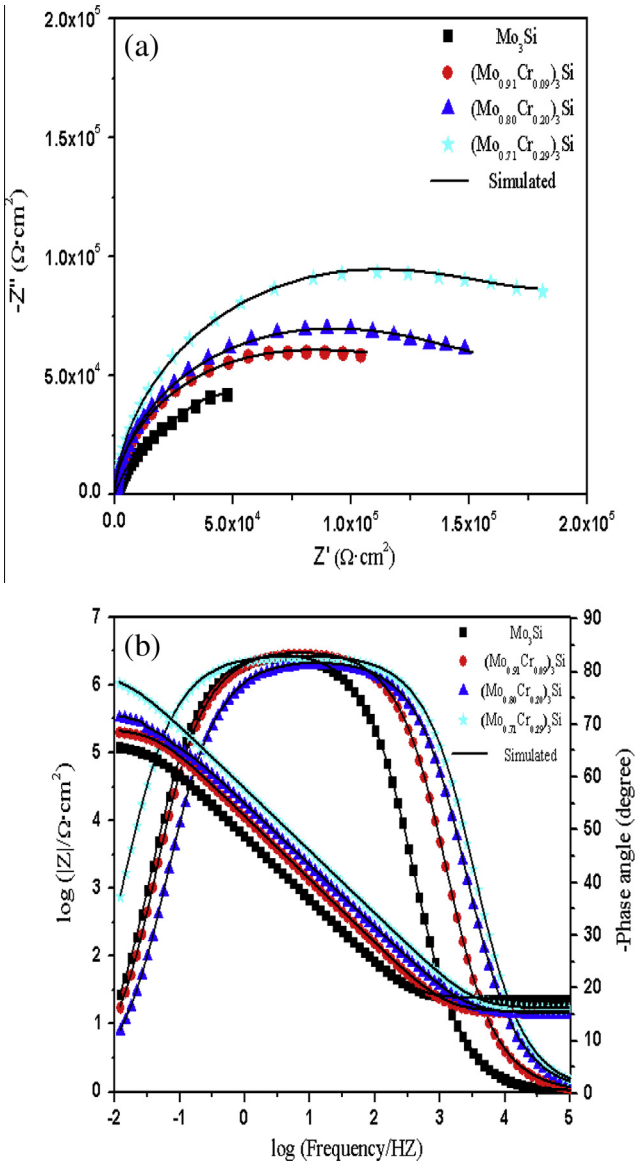

Fig. 11. (a) Nyquist plot and (b) Bode plot for the $(Mo_{1-x}Cr_x)_3Si$ nanocrystalline coatings in 3.5 wt% NaCl solution open to air at room temperature.

A modified Randles circuit (EEC) with one time constant model (Fig. 12) was adopted to fit the EIS experimental data. In the equivalent circuit [37], a solution resistance between working electrode and reference electrode, R_s, in series with the parallel combination of polarization resistance, R_p, and the constant phase element (Q_p or CPE) for the passive film. Taking the distributed relaxation feature of the electrode surface into consideration, a constant phase element (CPE) was used instead of an ideal capacitance for obtaining a best fit. The impedance of the CPE (Z_{CPE}) is expressed as $Z_{CPE} = [Q(j\omega)^n]^{-1}$, where Q is a constant, which represents the true capacitance of the passive film, ω is the angular frequency, j is the imaginary number and the factor n, defined as a CPE power, is an adjustable parameter that always lies between 0.5 and 1. The value of n is associated with the non-uniform distribution of current as a result of roughness and surface defects. When $n = 1$, the CPE acts like a capacitor with Q equal to the capacitance C; for $0.5 < n < 1$, the CPE describes a distribution of dielectric relaxation times in frequency domain; and when $n = 0.5$, the CPE represents a Warburg impedance with diffusion character. The simulated EIS parameters including R_s, R_p, Q_p and n using ZsimpWin software are summarized in Table 1. The chi-squared (χ^2) values of the order of 10^{-3}–10^{-4} indicate satisfactory agreement between the experimental and simulated data. As shown in Table 1, the polarization resistance (R_p) increases with an increase in Cr content in the coatings, whereas Q_p values exhibit the opposite trend. Furthermore, all the n values are larger than 0.9, and move closer to 1 with increasing Cr content, which acts more like an ideal capacitance for the passive films formed on the coatings. Potucek et al. [38] indicated that for the impedance measurements, the resistance (R) values obtained from EIS data are highly dependent on the solution selected, while the capacitance (C) values are immune to the effect of solution conditions and are, therefore, a much more reliable means for determining the related electrochemical properties of electrode. The values of effective capacitance (C) of the tested specimens can be converted from CPE values based on the criteria formulated by Brug et al. [39]:

$$C = Q^{1/n}\left[\frac{1}{R_s} + \frac{1}{R_p}\right]^{n-1/n} \quad (4)$$

It is clear that the capacitance values for the four $(Mo_{1-x}Cr_x)_3Si$ coatings vary inversely with Cr content in the coatings, suggesting that the insulating or dielectric properties of the passive films formed on the coatings are enhanced by Cr addition. Moreover, the time constant (τ), expressed as $\tau = C \times R_p$, can be used to describe the rate of relevant electrochemical process [40]. It can be seen from Table 1 that the values of the time constant (τ) for the four $(Mo_{1-x}Cr_x)_3Si$ coatings are proportional to Cr content in the coatings, indicating that Cr alloying has an obvious retarding effect on the charge transfer process in the passive film.

3.6. X-ray photoelectron spectroscopy analysis

To gain a deeper understanding of the effect of Cr additions on the electrochemical behavior of the four $(Mo_{1-x}Cr_x)_3Si$ coatings, it is essential to determine the chemical composition and chemical

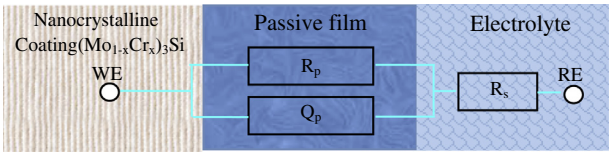

Fig. 12. Electrical equivalent circuit used to simulate the EIS data of the $(Mo_{1-x}Cr_x)_3Si$ nanocrystalline coatings in 3.5 wt% NaCl solution open to air at room temperature.

Table 1
Electrochemical parameters obtained from equivalent circuit simulation.

Sample	Mo_3Si	$(Mo_{0.91}Cr_{0.09})_3Si$	$(Mo_{0.80}Cr_{0.20})_3Si$	$(Mo_{0.71}Cr_{0.29})_3Si$
R_s (Ω cm^2)	13.65	14.08	15.12	16.25
Q_P (Ω^{-1} cm^{-2} s^n)	1.90×10^{-5}	1.51×10^{-5}	1.08×10^{-5}	0.65×10^{-5}
n	0.900	0.914	0.923	0.936
R_p (Ω cm^2)	1.49×10^5	2.14×10^5	5.18×10^5	1.44×10^6
C (μF cm^{-2})	7.59	7.09	5.58	3.87
χ^2	1.02×10^{-3}	1.83×10^{-3}	2.11×10^{-3}	4.32×10^{-3}
τ (s)	1.13	1.52	2.90	5.57

state of the elements in the passive films that are critical to the corrosion resistance of these coatings. XPS analysis was performed ex situ on the four $(Mo_{1-x}Cr_x)_3Si$ coatings after potentiostatic polarization at 0.1 V_{SCE} for 60 min in 3.5 wt% NaCl solution open to air. Fig. 13 shows XPS survey spectra for the passive films grown potentiostatically on the four $(Mo_{1-x}Cr_x)_3Si$ coatings. In the XPS spectra for the $(Mo_{1-x}Cr_x)_3Si$ coatings, Mo 3d, Si 2p, O 1s and C 1s core level principal peaks were observed for the Mo_3Si coating, while in addition these peaks, a Cr 2p peak was detected for the three Cr-containing Mo_3Si coatings and its intensity increased with increasing Cr addition. The C 1s peak at around 284.8 eV possibly arises from a contaminant hydrocarbon layer covering the specimen surface. Fig. 14 presents high-resolution XPS spectra for the Mo 3d, Cr 2p, Si 2p and O 1s peaks recorded from the passive film formed on the coatings. The Mo 3d spectra (Fig. 14(a)) consist of two doublet peaks from Mo $3d_{5/2}$ and Mo $3d_{3/2}$, which have been assigned to the Mo^{4+} state at 228.4 and 232.3 eV, and to metallic Mo at 227.6 and 231.6 eV [41]. Since metallic Mo may originate from the $(Mo_{1-x}Cr_x)_3Si$ coatings beneath the passive film, the primary Mo species in the film is a Mo^{4+} species with a binding energy equal to that of MoO_2. This phenomenon was also found by Halada et al. [42], who reported that metallic Mo is detected from variable angle XPS measurement of the passive film formed on pure Mo and $MoSi_2$ in deaerated 4 M HC1. The Cr 2p peaks (Fig. 14(b)) present one spin orbit doublets of Cr $2p_{3/2}$ and Cr $2p_{1/2}$ with respective binding energies of 576.3 and 586.8 eV, corresponding to Cr_2O_3. The Si 2p spectra in Fig. 14(c) exhibit one strong peak located at a binding energy of about 103.5 eV, corresponding to silicon in silicon dioxide (SiO_2) [43] and another peak at 99.3 eV, corresponding to elemental silicon. The O 1s spectra (Fig. 14(d)) can be decomposed into three peaks located at 531.2 eV, 532.6 eV and 533.0 eV. The centre of the peak (I) located at 531.2 eV may be attributed to a combination of Cr_2O_3 and MoO_2, since very small chemical shifts between them are difficult to distinguish among those metal oxides by core level XPS. The peak (II) at 532.6 eV arises from the OH^- ions and bound water in the surface film, which may be the adsorbed OH^- impurities on the sample surface from the ambient atmosphere [44,45]. The peak (III) at 533.0 eV can be attributed to the contribution from water (H–O–H) or to the Si–O bond corresponding to silicon oxides [46]. Fig. 15 presents the dominant constituent of the passive films formed on the four $(Mo_{1-x}Cr_x)_3Si$ coatings derived from quantitative evaluations of the deconvoluted spectra and the surface composition of the passive film determined using integrated intensities of XPS survey spectra after the removal of the signal from the C contamination. It is evident from Fig. 15 that the addition of Cr makes no difference to the amount of SiO_2, but decreases the concentration of MoO_2 accompanied by an increase of the concentration of Cr_2O_3 in the passive films.

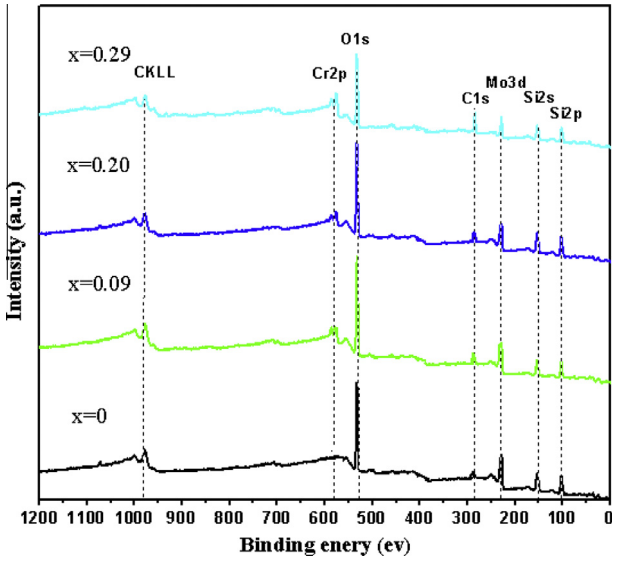

Fig. 13. XPS survey spectra of passive films on the $(Mo_{1-x}Cr_x)_3Si$ nanocrystalline coatings after potentiostatic polarization at 0.1 V_{SCE} for 60 min in 3.5% NaCl solution open to air at room temperature.

It is well known that the protective efficiency of the passive films is determined not only by their chemical composition, but also by their compactness in a variety of corrosive environments. A higher compactness imparts the passive film with a greater protective ability to obstruct the permeation of aggressive ions into the film [47]. In order to analyze the compactness of the passive film, the variation of current density with time for each specimen after cathodic reduction was measured at a fixed potential (0.10 V_{SCE}). If we neglect the contribution of the double layer charge, the initial fall of current density should be related to a film growth on the electrode surface [48]. The current density decreases with time according to the following relationship [49]:

$$i = 10^{-(A+k\lg t)} \quad (5)$$

where i represents the current density, t is time, A is constant and k represents the slope of the double-log plot for potentiostatic polarization, reflecting the compactness of the passive film. $k = -1$ indicates the formation of a compact, highly protective passive film, while $k = -0.5$ indicates the presence of a porous and diffusion-controlled film. Fig. 16 presents the double-log plots of current density-time for the four $(Mo_{1-x}Cr_x)_3Si$ coatings potentiostatically polarized at 0.1 V_{SCE}. As shown in Fig. 16, k values for the passive films grown on the coatings increase with Cr addition, implying that the compactness of passive film on the four $(Mo_{1-x}Cr_x)_3Si$ coatings can be improved by Cr additions.

4. Discussion

On the basis of the electrochemical test results, it can be concluded that that Cr alloying can considerably improve the corrosion resistance of a Mo_3Si nanocrystalline coating. To gain a deeper understanding of the corrosion mechanism at an atomic-level, the density of states (DOS) and Mulliken population of $(Mo_{1-x}Cr_x)_3Si$ were determined by first-principles calculations.

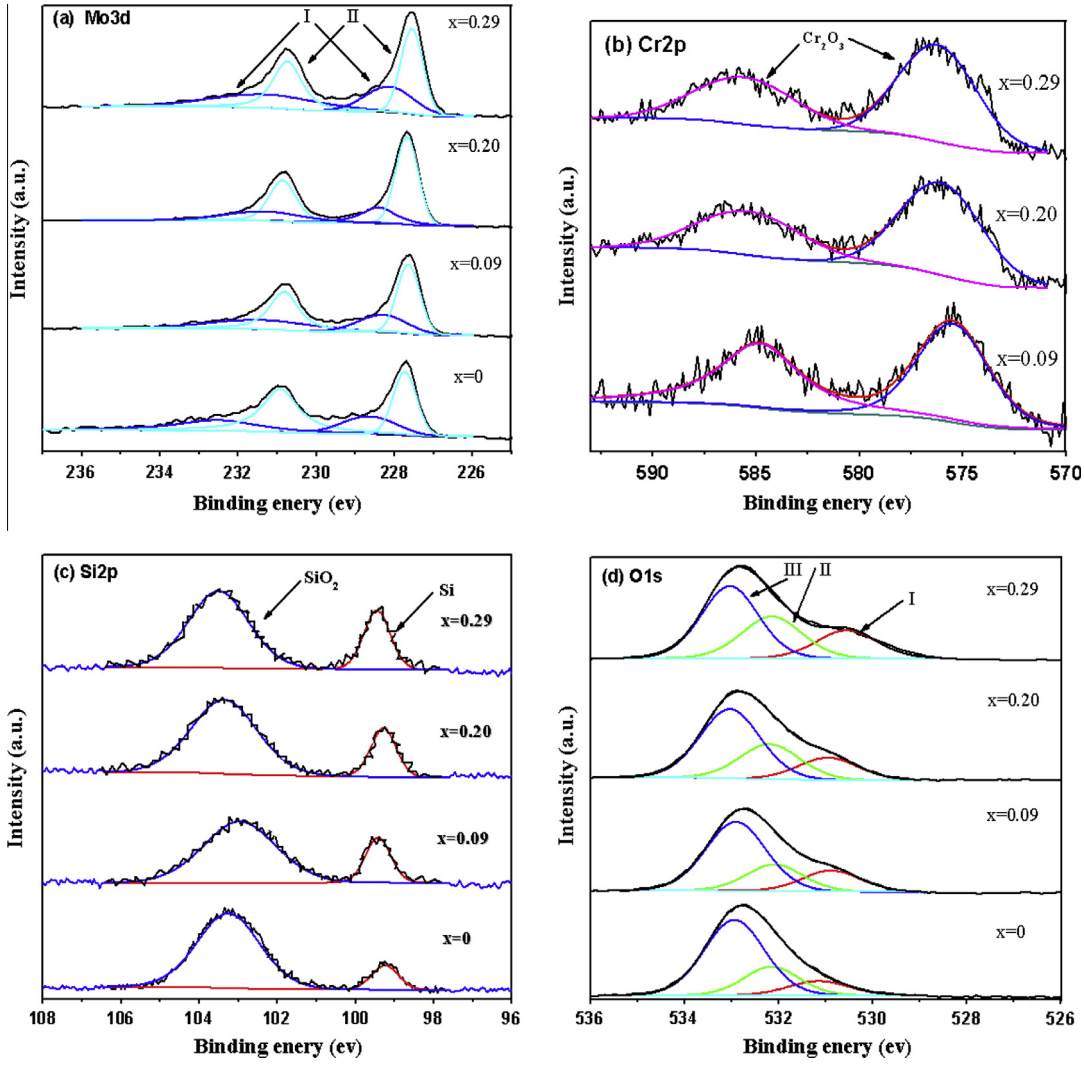

Fig. 14. Curve fitting of Mo 3d (a), Cr 2p (b), Si 2p (c) and O 1s (d) spectra for the $(Mo_{1-x}Cr_x)_3Si$ nanocrystalline coatings after potentiostatic polarization at 0.1 V_{SCE} for 60 min in 3.5% NaCl solution.

Fig. 17 shows the total densities of states (TDOS) and partial densities of states (PDOS) for $(Mo_{1-x}Cr_x)_3Si$. The Fermi level (E_F) is set at 0 eV. As shown in Fig. 17(a), the density of states for the binary Mo_3Si can be mainly divided into three parts. The first part extending from −10.5 eV to −8 eV originates from Si-s states with a minor contribution from Mo-d states. The second part from

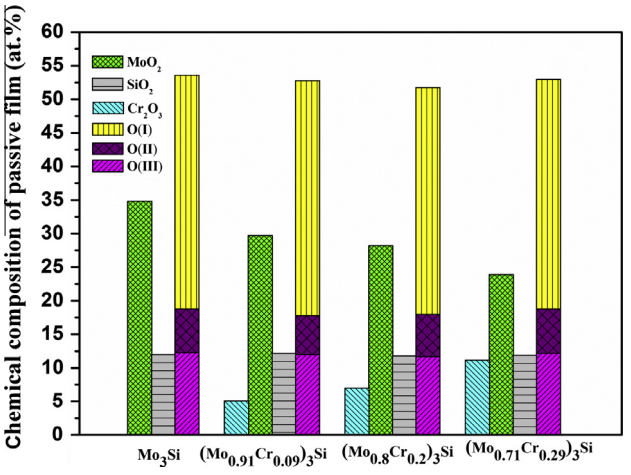

Fig. 15. The dominant constituent of the passive films formed on the $(Mo_{1-x}Cr_x)_3Si$ nanocrystalline coatings after potentiostatic polarization at a potential of 0.1 V_{SCE} for 60 min in 3.5 wt% NaCl solution open to air at room temperature.

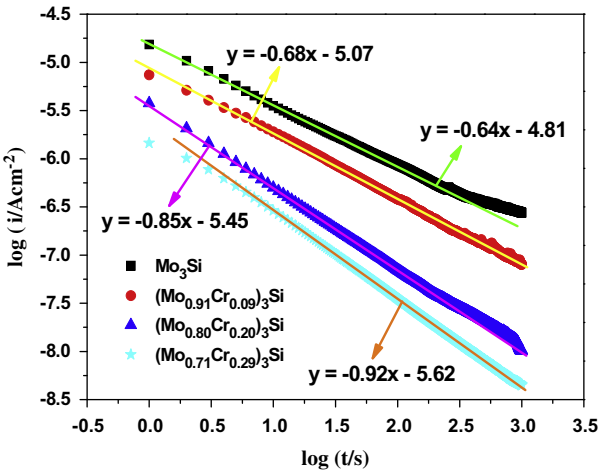

Fig. 16. Double-log plots of current–time for the $(Mo_{1-x}Cr_x)_3Si$ nanocrystalline coatings at 0.1 V_{SCE} in a 3.5 wt% NaCl solution.

−6.5 eV to −2.0 eV derives essentially from the contribution of Mo-d and Si-p states. The third part from −2.0 eV to 2 eV, is dominated by the Mo-d states. From the point view of bonding energy, the Mo–Si bonds are located in the lower energy level corresponding to a higher bonding strength, however, the Mo–Mo bonds extend into the higher energy level and, thus, exhibit weaker bonding. As shown in Fig. 17(b–d), the total density of states (TDOS) for the ternary $(Mo_{1-x}Cr_x)_3Si$ move to a higher energy level with increasing the concentration of Cr, suggesting that the strength of bonds in $(Mo_{1-x}Cr_x)_3Si$ is weaker than that of pure Mo_3Si. The Mo–Cr bonding states predominately occupy the higher energy level as compared to the Mo–Mo bonds and Mo–Si bonds, indicating that the Mo–Cr bonds have the weaker strength than other bonds in $(Mo_{1-x}Cr_x)_3Si$.

Furthermore, the relative strength of the chemical bonds in $(Mo_{1-x}Cr_x)_3Si$ can be also evaluated using Mulliken population analysis. In general, the larger the bond population, the stronger the bonds are [50]. Fig. 18 shows the variation of the Mulliken bond populations of $(Mo_{1-x}Cr_x)_3Si$ as a function of Cr addition. For the binary Mo_3Si crystal, either the strength of the Mo–Mo (I) or Mo–Mo (II) bonds, is obviously weaker than that of the Mo–Si bonds. However, when Cr atoms substitute Mo sublattice sites in the Mo_3Si crystal, some new bonds, such as Mo–Cr and Cr–Si bonds, appear in the ternary $(Mo_{1-x}Cr_x)_3Si$ crystal and a noticeable change in strength of bonds can be observed. For the ternary $(Mo_{1-x}Cr_x)_3Si$ crystal, strength of the Mo–Si, Cr–Si and Mo–Cr (I) bonds is markedly higher than that of the Mo–Mo (I), Mo–Mo (II) and Mo–Cr (II) bonds. It is worth noting that the addition of Cr to Mo_3Si weakens the strength of the Mo–Mo (I) and slightly increase the strength of Mo–Mo (II) bonds, all of which is larger than that of Mo–Cr (II) bonds. The results are in agreement with that of DOS analysis.

When the $(Mo_{1-x}Cr_x)_3Si$ coatings are exposed to corrosive electrolytes, the destructive chemical attack preferentially take place at the weakest bond amongst the different bonds that exist in the $(Mo_{1-x}Cr_x)_3Si$ crystal. According to DOS and Mulliken analyses, corrosion behavior of the binary Mo_3Si coating is primarily determined by the reaction between Mo–Mo (II) bonds and the NaCl

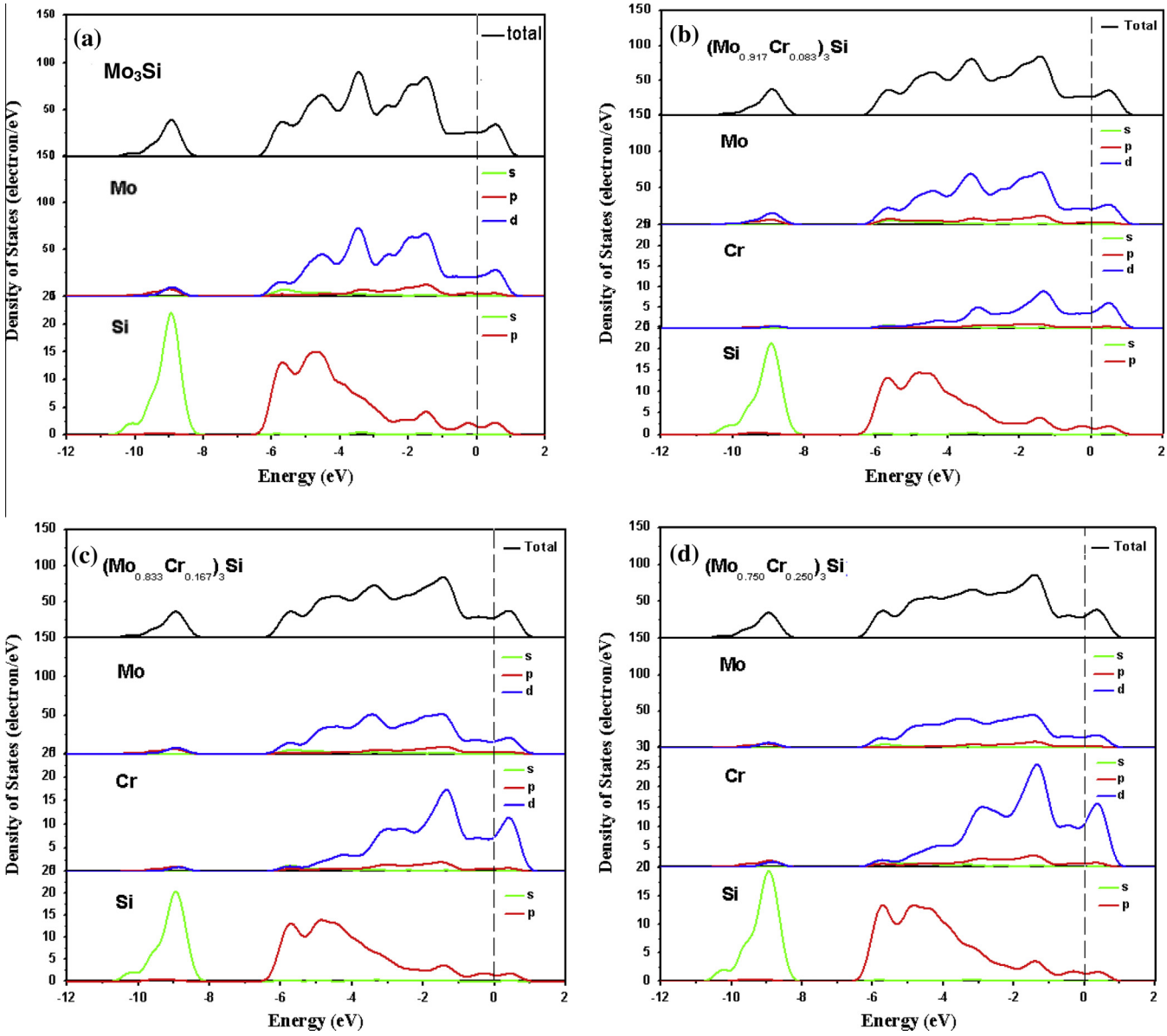

Fig. 17. Total and partial density of states of (a) Mo_3Si, (b) $(Mo_{0.917}Cr_{0.083})_3Si$, (c) $(Mo_{0.833}Cr_{0.167})_3Si$ and (d) $(Mo_{0.750}Cr_{0.250})_3Si$. The dotted lines represent the position of the Fermi level (E_F).

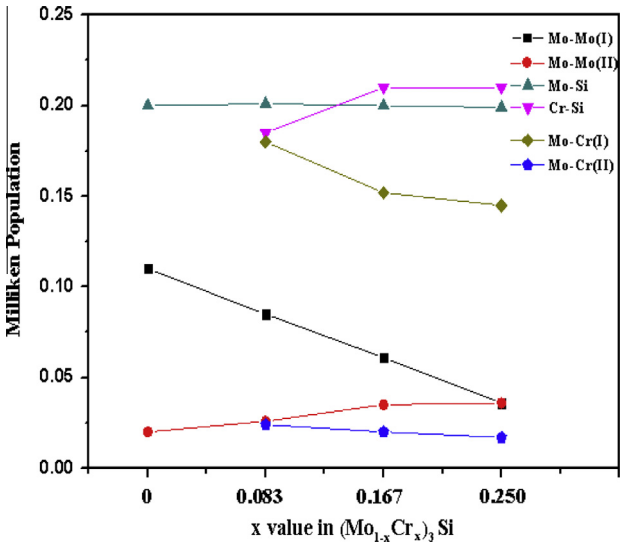

Fig. 18. Mulliken bond populations as a function of Cr content for $(Mo_{1-x}Cr_x)_3Si$.

solution. Based on theoretical potential–pH (E–pH) equilibrium diagram for the Mo–H_2O system at 25 °C, in the pH values of the solutions used here, the reaction product of Mo is MoO_2 in a low potential region, and the soluble product $HMoO_4^-$ is formed at a higher potential region. This result is consistent with that of the XPS measurements on the binary Mo_3Si coating. Therefore, during the electrochemical oxidation of molybdenum, the following possible electrode reactions may occur at surface of the binary Mo_3Si coating:

$$Mo + 2H_2O = MoO_2 + 4H^+ + 4e^- \quad (6)$$

$$MoO_2 + 2H_2O = HMoO^{4-} + 3H^+ + 2e^- \quad (7)$$

Because $HMoO4^-$ is a dissolution product, results in a non-protective film formed on the binary Mo_3Si coating in the transpassive region, the rate-determining step for the anodic dissolution reaction is Mo (IV) → Mo (VI). As shown in Fig. 18, the substitution of Cr for Mo in Mo_3Si causes an increase in the Mulliken population of Mo–Mo (II) bonds, enabling their strength to be higher than that of the Mo–Cr (II) bonds. On the contrary, for the ternary $(Mo_{1-x}Cr_x)_3Si$ coatings, the weakest Mo–Cr (II) bonds are preferentially broken when subjected to corrosion attack, and, thus, more Cr_2O_3 is incorporated into the passive film to improve the corrosion resistance of the underlying coatings.

5. Conclusion

In summary, four $(Mo_{1-x}Cr_x)_3Si$ ($x = 0$, 0.09, 0.20 and 0.29) nanocrystalline coatings with a cubic A15 structure were deposited onto Ti–6Al–4V substrates by a double-cathode glow discharge technique. All four as-deposited coatings exhibit a homogeneous and dense structure that consists of elongated grains with an average width of 10 nm. Cr additions lead to a change in preferred orientation from (2 1 0) to (2 0 0). The hardness and elastic modulus of the $(Mo_{1-x}Cr_x)_3Si$ coatings decreases with increasing Cr content, which is in agreement with the calculated results based on a first-principles density-functional theory. The abrasive wear resistance, however, is expected to increase with an increase in Cr content. The electrochemical test results reveal that Cr alloying improves the corrosion resistance of the as-deposited $(Mo_{1-x}Cr_x)_3Si$ coatings. Supported by analysis of electronic structure and Mulliken populations, it can be inferred that the lower corrosion resistance of the binary Mo_3Si results from the weaker Mo–Mo bonds that are preferentially broken during the corrosion process; however, for the ternary $(Mo_{1-x}Cr_x)_3Si$ coatings, the Cr addition increases the strength of Mo–Mo bonds, and the Mo–Cr (II) bonds have the weakest strength, which is favorable for the formation of a protective passive film on the coatings.

Acknowledgements

The authors acknowledge the financial support of the National Natural Science Foundation of China under Grant Nos. 51175245 and 51374130 and the Aeronautics Science Foundation of China under Grant No. 2013ZE52058.

References

[1] H. Katayama, S. Kuroda, Corros. Sci. 76 (2013) 35–41.
[2] H.M. Wang, G. Duan, Intermetallics 11 (2003) 755–762.
[3] J.J. Petrovic, Mater. Sci. Eng., A 192 (1995) 31–37.
[4] J. Pan, M.K. Surappa, R.A. Saravanan, B.W. Liu, Mater. Sci. Eng., A 244 (1998) 191–198.
[5] H. Fujiwara, Y. Ueda, J. Alloys Comp. 441 (2007) 168–173.
[6] A. Misra, J.J. Petrovic, T.E. Mitchell, Scr. Mater. 40 (2) (1999) 191–196.
[7] T. Dasgupta, A.M. Umarji, Intermetallics 15 (2007) 128–132.
[8] C.E. Ramberg, W.L. Worrell, J. Am. Ceram. Soc. 85 (2) (2002) 444–452.
[9] T. Dasgupta, A.M. Umarji, Intermetallics 16 (2008) 739–744.
[10] I. Rosales, D. Bahena, Mater. Sci. Eng., A 459 (2007) 132–136.
[11] I. Rosales, H. Martinez, D. Ponce, J.A. Ruiz, Int. J. Refract. Metal Hard Mater. 25 (2007) 250–255.
[12] I. Rosales, J.H. Schneibel, Intermetallics 8 (2000) 885–889.
[13] J. Xu, D.H. Lai, Z.H. Xie, P. Munroe, J. Mater. Chem. 22 (2012) 2596–2606.
[14] J. Xu, X.Z. Mao, Z.H. Xie, J. Phys. Chem. C 115 (39) (2011) 18977–18982.
[15] J. Xu, Y. Wang, S.Y. Jiang, Nanoscale 2 (2010) 394–398.
[16] J. Xu, S.Y. Jiang, Y. Wang, ACS Appl. Mater. Interfaces 2 (1) (2010) 301–311.
[17] W.C. Oliver, G.M. Pharr, J. Mater. Res. 7 (1992) 1565–1583.
[18] W. Du, L.Q. Zhang, F. Ye, Phys. Rev. B: Condens. Matter 405 (2010) 1695–1700.
[19] D.H. Lai, J. Xu, Z.H. Xie, Mater. Charact. 68 (2012) 1–6.
[20] H.J. Monkhorst, J.D. Pack, Phys. Rev. B 13 (1976) 5188–5192.
[21] K.R. Babu, C.B. Lingam, S. Auluck, J. Solid State Chem. 184 (2011) 343–350.
[22] T. Chihi, M. Fatmi, M.A. Ghebouli, Phys. Rev. B: Condens. Matter 407 (2012) 3591–3595.
[23] Z.J. Chen, D.B. Tian, J. Appl. Phys. 109 (2011). 033506-033506-5.
[24] M.I. Jones, I.R. McColl, D.M. Gran, Surf. Coat. Technol. 132 (2000) 143–151.
[25] C.Y. Su, C.T. Lu, W.T. Hsiao, W.H. Liu, Thin Solid Films 544 (2013) 170–174.
[26] K. Ashok, B. Subramanian, P. Kuppusami, M. Jayachandran, Cryst. Res. Technol. 44 (2009) 511–516.
[27] T. Elangovan, P. Kuppusami, R. Thirumurugesan, Mater. Sci. Eng., B 167 (2010) 17–25.
[28] J.C. Weaver, Q.Q. Wang, A. Miserez, Mater. Today 13 (2010) 42–52.
[29] H. Hou, Z.Q. Wen, Y.H. Zhao, L. Fu, Intermetallics 44 (2014) 110–115.
[30] U.R. Evans, The Corrosion of Metals, Edward Arnold, London, 1960, p. 898.
[31] M.A. Amin, M.A. Ahmed, H.A. Arida, Corros. Sci. 53 (2011) 1895–1909.
[32] J. Kittel, N. Celati, Prog. Org. Coat. 46 (2) (2003) 135–147.
[33] S.L. Assis, I. Costa, Mater. Corros. 58 (2007) 329–333.
[34] S. Tamilselvi, V. Raman, N. Rajendran, Electrochim. Acta 52 (2006) 839–846.
[35] I.C. Lavos-Valereto, S. Wolynec, I. Ramires, J. Mater. Sci. – Mater. Med. 15 (2004) 55–59.
[36] V.A. Alves, R.Q. Reis, I.C.B. Santos, Corros. Sci. 51 (2009) 2473–2482.
[37] J.R. Macdonald, editor, Impedance spectroscopy–Emphasizing solid materials and systems. New York: Wiley-Interscience, 1987.
[38] R.K. Potucek, R.G. Rateick, V.I. Birss, J. Chem. Soc. 153 (2006) B304–B310.
[39] G.J. Brug, A.L.G. Van Den Eeden, M. Sluyters-Rehbach, J.H. Sluyters, J. Electroanal. Chem. 176 (1984) 275–295.
[40] A. Petrossians, J.J. Whalen, J.D. Weiland, F. Mansfeld, J. Electrochem. Soc. 158 (2011) D269–D276.
[41] L.Q. Wang, L.F. Jiao, H.T. Yuan, J. Power Sources 162 (2006) 1367–1372.
[42] G.P. Halada, C.R. Clayton, H. Herman, S. Sampath, R. Tiwari, J. Electrochem. Soc. 142 (1995) 74–80.
[43] J. Zhao, J. Li, P.L. Ying, Chem. Commun. 49 (2013) 4477–4479.
[44] K.M. Ismail, A.A. El-Moneim, W.A. Badawy, J. Electrochem. Soc., J. Electrochem. Soc. 148 (2001) C81–C87.
[45] B.S. Yang, M.S. Huh, O. Seungha, U.S. Lee, Appl. Phys. Lett. 98 (2011). 122110-122110-3.
[46] T. Matsutani, T. Asanuma, C. Liu, M. Kiuchi, T. Takeuchi, Surf. Coat. Technol. 177 (2004) 365–368.
[47] L.L. Liu, J. Xu, Z.H. Xie, P. Munroe, J. Mater. Chem. A 1 (2013) 2064–2078.
[48] J.R. Galvele, R.M. Torresi, R.M. Carranza, Corros. Sci. 31 (1990) 563–571.
[49] H.H. Hassan, Electrochim. Acta 51 (2005) 526–535.
[50] X.Y. Zhao, Y.H. Wang, Q. Chen, Comput. Mater. Sci. 54 (2012) 119–124.